

A Transformer-Conditioned Neural Fields Pipeline with Polar Coordinate Representation for Astronomical Radio Interferometric Data Reconstruction

Ruoqi Wang

The Hong Kong University of
Science and Technology (Guangzhou)
rwang280@connect.hkust.edu.cn

Qiong Luo

The Hong Kong University of
Science and Technology (Guangzhou)
luo@cse.ust.hk

Feng Wang

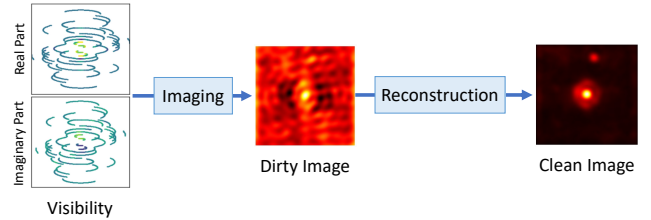
Guangzhou University
fengwang@gzhu.edu.cn

Abstract

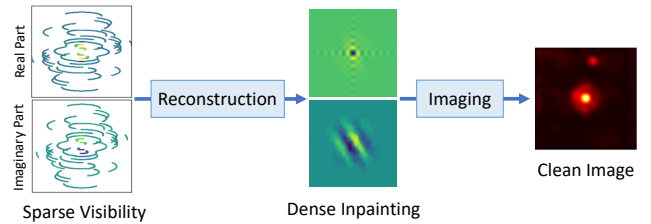
In radio astronomy, visibility data, which are measurements of wave signals from radio telescopes, are transformed into images for observation of distant celestial objects. However, these resultant images usually contain both real sources and artifacts, due to signal sparsity and other factors. One way to obtain cleaner images is to reconstruct samples into dense forms before imaging. Unfortunately, existing visibility reconstruction methods may miss some components of the frequency data, so blurred object edges and persistent artifacts remain in the images. Furthermore, the computation overhead is high on irregular visibility samples due to the data skew. To address these problems, we propose PolarRec, a reconstruction method for interferometric visibility data, which consists of a transformer-conditioned neural fields pipeline with a polar coordinate representation. This representation matches the way in which telescopes observe a celestial area as the Earth rotates. We further propose Radial Frequency Loss function, using radial coordinates in the polar coordinate system to correlate with the frequency information, to help reconstruct complete visibility. We also group visibility sample points by angular coordinates in the polar coordinate system, and use groups as the granularity for subsequent encoding with a Transformer encoder. Consequently, our method can capture the inherent characteristics of visibility data effectively and efficiently. Our experiments demonstrate that PolarRec markedly improves imaging results by faithfully reconstructing all frequency components in the visibility domain while significantly reducing the computation cost.

Introduction

In radio astronomy, *visibility* refers to radio signal data from celestial objects, obtained by radio telescopes. These data are represented as complex values in the *uv-plane*, a geometric plane defined for interferometric observations. Visibility data are subsequently converted into images through *imaging* for further analysis. However, these images, known as *dirty images*, are often dominated by artifacts (Schmidt et al. 2022). This phenomenon is due to limitations in telescope configurations, under which not the entire *uv-plane* is sampled. Therefore, visibility data normally have to be reconstructed before being utilized in scientific analysis. In this paper, we propose a visibility reconstruction method,



(a) Traditional method: imaging followed by reconstruction



(b) Recent method: reconstruction followed by imaging

Figure 1: Two visibility data processing flows.

aiming to reconstruct the real sky by recovering all visibility components in the *uv-plane* effectively and efficiently.

Traditional methods first transfer the sparse visibility data into dirty images through the imaging process and then reconstruct the dirty images to *clean images*. The process is shown in Figure 1 (a). In contrast, some recent deep-learning-based studies (Schmidt et al. 2022; Wu et al. 2022) have proposed to first do inpainting on the visibility data to reconstruct the sparse samples to dense coverage, and then perform imaging to obtain the clean image, as shown in Figure 1 (b). In order to produce a high-fidelity sharp image, it is crucial to densely sample the full visibility domain (Wu et al. 2022). In this paper, we adopt the reconstruction-and-imaging processing flow.

Existing methods for reconstructing visibility data face challenges in both effectiveness and efficiency. Specifically, the first challenge is to effectively capture all visibility components within the *uv-plane*. For example, Radionets (Schmidt et al. 2022) use a convolutional neural network that is based on pixels and grids, resulting in discontinuous information in the reconstructed visibility. In comparison, Wu et al. (Wu et al. 2022) use neural fields to address the conti-

nuity problem, but their method can accurately restore the low-frequency part of visibility only (located near the center of the uv-plane), largely missing the high-frequency portion (found far from the uv-plane center). Such discontinuity and incompleteness in the visibility domain result in blurred edges of observed objects, disappearance of faint astronomical sources, and persistence of artifacts, in resultant images. The second major issue is the inefficiency of current strategies. For instance, Radionets (Schmidt et al. 2022) encode visibility data together with an excessive amount of zero-inpainting, causing a large amount of unnecessary computation. Wu et al. (Wu et al. 2022) embed each visibility sample point as a token in their Transformer encoder (Vaswani et al. 2017) to attend to each other, which is of quadratic computation cost in the number of sample points, too high for real applications (Dosovitskiy et al. 2021).

To address these challenges, we explore the impact of different frequency components of visibility on imaging results and then propose PolarRec, which leverages the polar representation of sample points to enhance the reconstruction performance. Our key observation is that high- and low-frequency signals are distributed on the uv-plane in accordance with their distances from the center and visibility samples are obtained by telescopes as the Earth rotates. Therefore, we propose to use the radial coordinate to associate with the frequency information and the angular coordinate to group sample points, both in the polar coordinate system.

Specifically, we design a weighting scheme based on the radial coordinates of visibility points and integrate our weighting scheme with the Focal Frequency Loss function (Jiang et al. 2021). Our weighted loss function, Radial Frequency Loss, associates frequency with radial coordinates, enabling effective reconstruction of visibility data, on both high- and low-frequency components, whereas existing work recovers mainly low-frequency components. Consequently, our method produces sharper, more detailed imaging results. Furthermore, by grouping visibility points according to their angular coordinates and performing encoding at the group level, our Transformer encoder is more efficient than single-visibility-point encoding since each group of visibility points is processed to be one token for the Transformer encoder. This group encoding improves computation efficiency, making the use of Transformer encoders for visibility encoding more practical and scalable.

In summary, our main contributions are as follows:

- We propose Radial Frequency Loss (RFL) function, which incorporates the radial coordinate in the polar representation of visibility data. This approach enables the model to effectively capture the complete visibility data, especially the high-frequency components.
- We design an intuitive and effective grouping method based on the angular coordinate in the polar representation of visibility data. Utilizing these angular groups as the granularity for subsequent encoding by the Transformer improves computation efficiency significantly.

We have experimentally evaluated our proposed PolarRec, including an overall comparison with other state-of-the-art methods, ablation studies on individual weighting

techniques, and tests on group sizes and grouping techniques. Our experimental results confirm that our method can faithfully reconstruct all frequency components of visibility, significantly enhancing the quality of the resultant images. Also, our method effectively reduces the computation cost of visibility encoding while preserving the high quality of resultant images. This efficiency improvement makes it more practical to use Transformer encoders for visibility data encoding in real-world applications.

Background and Related Work

Very Long Baseline Interferometry (VLBI)

In radio astronomy, using radio interference signals to image distant astronomical sources requires telescopes of very large aperture (Bouman et al. 2018), because the angular resolution of a telescope is inversely proportional to the diameter. A major observation technique is the Very Long Baseline Interferometry (VLBI), which uses multiple radio telescopes spreading over the globe to form a virtual Earth-sized telescope. The radio waves from astronomical sources are recorded separately at individual telescopes. Then, these signals are cross-correlated for all pairs of antennas at a central location, generating *visibility* data. A VLBI observation is typically performed for hours to measure as many points in the uv-plane as possible. However, the measurement results remain sparse due to the limited number of antennas (Thompson, Moran, and Swenson 2017; Bouman et al. 2018). Consequently, sparse-to-dense reconstruction on visibility data is necessary to improve the imaging quality.

Interferometric Imaging

Visibility data, represented as complex values, is the result of a Fourier transform of the sky’s brightness distribution (Liu, Luo, and Wang 2022). *Imaging* converts visibility data into images, which can be analyzed to provide insights about the observed celestial bodies (Thompson, Moran, and Swenson 2017). In the imaging process, an inverse Fourier transform maps the (u, v) coordinates from the Fourier domain to (l, m) coordinates in the image domain (Wu et al. 2022). The transformation can be described as:

$$I(l, m) = \int_u \int_v e^{2\pi i(ul+vm)} V(u, v) dudv. \quad (1)$$

In this equation, $V(u, v)$ is the visibility data in Fourier space, and $I(l, m)$ represents the intensity distribution in the image domain.

Radio Interferometric Data Reconstruction

The number of radio antennas in VLBI is limited and the antennas are non-uniformly distributed on the ground. As a result, visibility data are sparsely sampled and irregularly scattered (Thompson, Moran, and Swenson 2017; Bouman et al. 2018). When the inverse Fourier transform is applied to this sparse data, the resultant dirty image is dominated by artifacts (Schmidt et al. 2022). Therefore, these data must be further reconstructed to recover the real sky for subsequent scientific analysis (Wu et al. 2022).

There are two ways to reconstruct radio interferometric data to obtain clean images, reconstruction in the visibility domain and reconstruction in the image domain. A number of existing methods (Högbom 1974; Ables 1974; Bouman et al. 2016; Sun and Bouman 2021; Connor et al. 2022) first do imaging to transfer the sparse visibility into dirty images and then reconstruct the dirty images to clean images. Most recently two papers have proposed to perform sparse-to-dense inpainting in the visibility domain first and then do imaging (Wu et al. 2022; Schmidt et al. 2022). Specifically, Schmidt et al. (Schmidt et al. 2022) used Radionets with a convolutional neural network structure to generate reproducible clean images on simulated data, whereas Wu et al. (Wu et al. 2022) performed sparse-to-dense inpainting in the spectral domain with neural fields, outperforming other established reconstruction techniques.

In our experiments, we employed various state-of-the-art deep learning methods for visibility reconstruction (Wu et al. 2022; Schmidt et al. 2022; Ronneberger, Fischer, and Brox 2015). We found that these approaches could successfully recover the general structure of the most prominent object. However, certain details and faint surrounding sources were missing, and some artifacts persisted in the reconstructed images. These limitations are due to the incomplete reconstruction of visibility components. For example, both Radionets (Schmidt et al. 2022) and U-Nets (Ronneberger, Fischer, and Brox 2015) were based on pixels and grids, so the reconstruction of visibility data was not continuous. In comparison, Wu et al. used Neural Interferometry (Wu et al. 2022) to reconstruct continuous visibility, but it could recover the low-frequency components only, missing the high-frequency ones. Furthermore, embedding each visibility point as a token results in a large number of tokens to be processed by the Transformer encoder, leading to a quadratic increase of computation cost (Wu et al. 2022). To the best of our knowledge, no previous studies have managed to reconstruct all components in visibility data or increase the granularity of visibility data by Transformer encoders for efficiency.

Our Method

In this section, we first investigate the relation between visibility components and corresponding imaging results. After that, we present PolarRec, which adopts polar coordi-

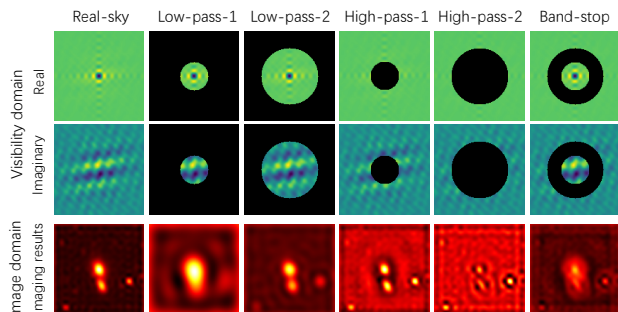


Figure 2: Effects of band limiting.

nate representation in visibility reconstruction. In PolarRec, we design Radial Frequency Loss to incorporate a weighting scheme based on the radial coordinate within the uv-plane. Moreover, we group the visibility points according to their angular coordinates and then extract grouping tokens for the subsequent Transformer encoding. An overview of our method is presented in Figure 3.

Imaging Results of Visibility

In radio interferometry, visibility data plays a vital role in generating high-fidelity images of celestial objects. The imaging process is the inverse Fourier transformation of visibility data to construct the brightness distribution of the observed sky. Consequently, missing or incomplete visibility components can significantly degrade the imaging result, leading to artifacts and loss of crucial information about the object’s structure. Therefore, we first investigate the impact of missing visibility components on the final imaging output.

We explore the impact of visibility components in various frequency regions by applying standard band-limiting operations (Jiang et al. 2021) and analyzing the effects of individual components on the imaging results. As shown in Figure 2), loss of high frequency data due to a low-pass filter (Column low-pass-1 and low-pass-2) results in blur and artifacts and causes the vanishing of weak sources in the imaging results. Comparing low-pass-1 and low-pass-2, we can see that the larger the radius of the retained portion in the frequency domain, the clearer the resulting image is, and the fewer artifacts there are. In comparison, when low frequency data are absent due to a high-pass filter (Column high-pass-1 and high-pass-2), the overall quality of the image declines, but the object edges are clear, and dim or small sources around the main observed object are retained. Last, the band-and-stop filter (Column Band-stop) also causes artifacts and blur in imaging results.

In summary, different frequency regions cause distinct imaging effects. This observation suggests that recovering all missing visibility components could enhance the quality of imaging result. More specifically, if a resultant image has blurred edges or misses dim light sources, it is probably due to poor reconstruction of the high-frequency components of the visibility data.

Polar Coordinate Representation

Our utilization of the polar coordinate representation is a natural and intuitive approach, because visibility sampling is based on Earth’s rotation and high- and low-frequency visibility components are distributed on the uv-plane according to their distances from the origin of the plane.

In the uv-plane, we convert (u, v) coordinates to polar coordinates, denoted as $(r(u, v), \theta(u, v))$:

$$r(u, v) = \sqrt{u^2 + v^2} \quad (2)$$

$$\theta(u, v) = \arctan2(v, u) \quad (3)$$

Where $r(u, v)$ represents the radial distance from the origin, and $\theta(u, v)$ represents the angle of the vector from the positive u -axis.

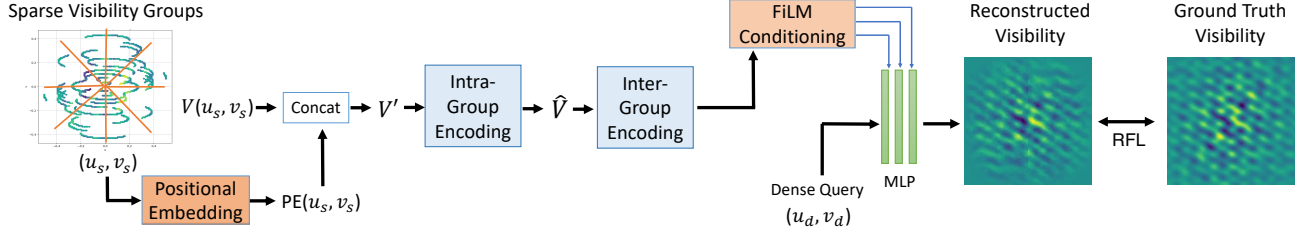


Figure 3: An overview of our method. Sparse visibility data $V(u_s, v_s)$ are grouped by the angular coordinate and concatenated with positional embedding $PE(u_s, v_s)$ to obtain V' . Then V' passes through two encoding layers: intra-group encoding to generate group tokens and inter-group encoding by a Transformer encoder. The encoded output then conditions the predicted visibility generation in the neural field. The final output is compared with the ground truth to compute the Radial Frequency Loss.

Radial Frequency Loss

Our Radial Frequency Loss (RFL) is built upon the Focal Frequency Loss (FFL) (Jiang et al. 2021). Based on FFL (Jiang et al. 2021), we compute the weight matrix $w_1(u, v)$ to down-weight easy visibility components (components whose predicted values are close to ground truth):

$$w_1(u, v) = |V_r(u, v) - V_p(u, v)|^\alpha \quad (4)$$

where $V_r(u, v)$ and $V_p(u, v)$ represent the real and predicted visibility respectively, and α is a scaling factor.

We introduce an additional weight $w_2(u, v)$, computed from $r(u, v)$, to make our model pay more attention to high-frequency components of the visibility during reconstruction. The weight term $w_2(u, v)$ is calculated as follows:

$$w_2(u, v) = \left(\frac{r(u, v)}{\max(r(u, v))} + 1 \right)^\beta \quad (5)$$

Where $\frac{r(u, v)}{\max(r(u, v))}$ normalizes the radial coordinate, ensuring the weight is more significant for points farther from the center, corresponding to higher frequencies in the visibility data. Adding 1 prevents any weights from becoming zero, maintaining the influence of all visibility components during the learning process. β is a scaling factor.

The final weight $w(u, v)$ is computed as:

$$w(u, v) = \left(\frac{r(u, v)}{\max(r(u, v))} + 1 \right)^\beta |V_r(u, v) - V_p(u, v)|^\alpha \quad (6)$$

The final form of the Radial Frequency Loss is then given by:

$$\text{RFL} = \frac{1}{MN} \sum_{u=0}^{M-1} \sum_{v=0}^{N-1} w(u, v) |V_r(u, v) - V_p(u, v)|^2 \quad (7)$$

Encoding by Angular-Coordinate-Based Groups

As shown on the left in Figure 3, the sparsely sampled visibility data is in the form of $\{u_s, v_s, V(u_s, v_s)\}$, where (u_s, v_s) are the coordinates at which a measurement is sampled and $V(u_s, v_s)$ is the complex value of the sample points.

First, we divide the sample points into m groups according to their angular coordinate $\theta(u_s, v_s)$, as shown on the left of Figure 3. To integrate each visibility value and its corresponding position, we encode each sample individually using positional embedding ($PE(u_s, v_s)$ in Figure 3). Specifically, we encode the positional information of a sample point using Random Fourier Embedding (Tancik et al. 2020). After that, the positional embedding $PE(u_s, v_s)$ and the embedding of complex value of visibility $V(u_s, v_s)$ are concatenated to form visibility tokens V' . Denote the sparse visibility tokens as $V' = [v'_1; v'_2; v'_3; \dots; v'_n]$, where $V' \in \mathbb{R}^{n \times d}$, n is the number of sample measurement points and d is the number of dimensions of visibility tokens.

Then, we apply a Multi-Layer Perceptron (MLP) mapping layer and averaging aggregating for intra-group encoding, as shown in the middle of Figure 3. The encoding result is $\hat{V} = [\hat{v}_1; \hat{v}_2; \hat{v}_3; \dots; \hat{v}_m]$, where $\hat{V} \in \mathbb{R}^{m \times d}$.

For each group i , we compute the group token \hat{v}_i as follows:

$$\hat{v}_i = \text{Avg}(\text{MLP}(v_j)), \quad i = 1 \text{ to } m, \quad v_j \in \text{group } i. \quad (8)$$

In intra-group encoding (Algorithm 1), we first sort the tokens V' of sample points according to their angular coordinates. After mapping these tokens through MLP, we use adaptive average pooling to compute the group tokens \hat{V} . For data collected with the same telescope configuration, the process of sorting based on angular coordinates needs to be performed only once, as the locations of sample points remain unchanged.

Algorithm 1 Intra-Group Encoding

- 1: Given input tokens V'
 - 2: $V'' \leftarrow \text{SortByAngle}(V', \theta(u, v))$
 - 3: $V^{\text{MLP}} \leftarrow \text{MLP}(V'')$
 - 4: $\hat{V} \leftarrow \text{AdaptiveAvgPooling}(V^{\text{MLP}}, m)$
 - 5: **return** \hat{V}
-

Finally, the group tokens \hat{V} go through inter-group encoding by a Transformer encoder. We base our encoder design on Transformer structures similar to prior work (Vaswani et

al. 2017; Dosovitskiy et al. 2021; Wu et al. 2022). The input group tokens are then transformed into latent tokens by multi-headed self-attention layers.

Neural Field Conditioning

Our method follows the conditional neural field pipeline proposed by Wu et al. (Wu et al. 2022). Given the sparsely sampled visibility $V(u_s, v_s)$, our objective is to determine a neural field Φ , fulfilling a constraint set by the function F :

$$F(\Phi(u_s, v_s), V(u_s, v_s)) = 0. \quad (9)$$

We approximate this implicit function $\Phi(u, v)$ with an MLP of l layers parameterized by weights Θ_m .

We use the output tokens of inter-group encoding $T = [t_1; t_2; t_3; \dots t_l]$ to extend the neural field with a learning-based prior, with each token corresponding to an MLP layer. Using the FiLM conditioning (Perez et al. 2018), the output tokens modulate the i th layer’s activation \mathbf{x}_i by:

$$\text{FiLM}(\mathbf{x}_i) = \gamma(t_i) \odot \mathbf{x}_i + \beta(t_i), i \in 1 \text{ to } l, \quad (10)$$

where γ and β are simple affine layers with non-linearities and \odot signifies a Hadamard product (Horn 1990).

The MLP parameters Θ_m and the encoder parameters Θ_e are jointly optimized during training:

$$\begin{aligned} \min_{\Theta_m, \Theta_e} \text{RFL}(\Phi(u_d, v_d; \{T\}; \Theta_m), V_{\text{gt}}(u_d, v_d)), \\ \text{with } \{T\} = \Psi(\{u_s, v_s, V(u_s, v_s)\}; \Theta_e), \end{aligned} \quad (11)$$

where (u_d, v_d) are the dense coordinates in visibility plane and $V_{\text{gt}}(u_d, v_d)$ is the ground truth of visibility inpainting.

Experiments

In this section, we conduct a comprehensive evaluation of our method in comparison with several classic and recent state-of-the-art methods to demonstrate the overall improvement achieved by our approach. We also designed experiments to explore the effects of different grouping methods and group sizes on the reconstruction results. In addition, we conduct ablation experiments to study the effects of individual weighting techniques in RFL.

Experimental Setup

Platform. We conduct all experiments on a server with two AMD EPYC 7302 CPUs, 128GB main memory, and eight Nvidia RTX 3090 GPUs each with 24GB device memory. The server is equipped with an NVME 2TB SSD and four 1TB SATA hard disks. The operating system is Ubuntu 20.04. Our model is implemented in PyTorch 1.8.1 (Paszke et al. 2019).

Datasets. In our studies, we use the Galaxy10 DECals dataset (Henry 2021), consistent with the latest research in astronomical interferometric visibility reconstruction (Wu et al. 2022). This dataset comprises 17,736 galaxy images, sourced from the DESI Legacy Imaging Surveys (Dey et al. 2019). This in turn, merges data from the Beijing-Arizona Sky Survey (BASS) (Zou et al. 2017), the DECam Legacy Survey (DECaLS) (Blum et al. 2016), and the Mayall z-band Legacy Survey (Silva et al. 2016). Using these images as a

reference, we employ the eht-imaging toolkit (Chael et al. 2019; Chael et al. 2018) to produce visibility data represented by $\{u_s, v_s, V(u_s, v_s)\}$. The parameters for observation were adjusted to mirror an 8-telescope Event Horizon Telescope (EHT) setup (Wu et al. 2022), with the EHT being one of the most prominent arrays leveraging VLBI techniques. Each image has 1660 visibility points sampled and the image dimensions are set at 256×256 pixels. Following the methods of Wu et al. (Wu et al. 2022), we apply the discrete Fourier transform (DFT) technique to create dirty images out of the visibility data. We then randomly split 5000 images for testing, with the remainder being used for training.

Implementation Details. We use a 2-layer MLP with a Leaky ReLU activation in the intra-group encoder. We then use an 8-layer MLP in the neural field, and only the first 8 output tokens with the dimension of 1024 from the Transformer encoder are used to condition this 8-layer MLP. The two scaling factors α and β in the Radial Frequency Loss are both set to 1.

Methods under Comparison. We compare our method with three other methods for radio interferometry reconstruction, including the classic method CLEAN (Högbom 1974), which is for dirty image reconstruction, and two recent deep learning-based approaches for visibility data reconstruction – Radionets (Schmidt et al. 2022) and Neural Interferometry (Wu et al. 2022). We use the original code of these methods and follow the parameter setting in the original code for the best performance. All these methods are implemented on PyTorch. In addition, we test the U-Net (Ronneberger, Fischer, and Brox 2015) to reconstruct visibility data as supplementary baselines.

Evaluation Metrics. To measure differences in frequency data, we use the Log Frequency Distance (LFD) (Jiang et al. 2021), which is defined as follows:

$$\text{LFD} = \log \left[\frac{1}{MN} \left(\sum_{u=0}^{M-1} \sum_{v=0}^{N-1} |V_r(u, v) - V_p(u, v)|^2 \right) + 1 \right] \quad (12)$$

where $V_r(u, v)$ and $V_p(u, v)$ represent the real and predicted visibility respectively. A lower LFD is better.

To evaluate the quality of images after imaging the reconstructed visibility, we employ two common metrics: Peak Signal-to-Noise Ratio (PSNR) and Structural Similarity Index Measure (SSIM). PSNR quantifies the overall image quality of the resultant images, and SSIM quantifies the perceptual similarity to the ground truth images. We compute these two metrics using the scikit-image package (Singh and Singh 2019), which follows the formulas presented by Hore et al. (Hore and Ziou 2010). A higher PSNR and SSIM is better.

To evaluate the efficiency, we use inference time and Floating Point Operations (FLOPs). The inference time in the experiments is for a batch size of 32 on a single Nvidia RTX 3090. The FLOPs number is also computed in the same setting. We compare time performance between our method and Neural Interferometry only, because only these two are transformer-encoder based.

Table 1: Overall performance comparison.

Models	Domain		Metrics		
	Img	Vis	LFD↓	PSNR↑	SSIM↑
Dirty			N/A	10.204 ± 1.079	0.6583 ± 0.0543
CLEAN	✓		N/A	17.535 ± 2.195	0.8023 ± 0.0304
U-Net		✓	1.465 ± 0.318	16.175 ± 1.952	0.7814 ± 0.0323
Radionets		✓	1.173 ± 0.262	19.575 ± 2.350	0.8305 ± 0.0300
Neural Interferometry		✓	0.962 ± 0.320	22.956 ± 2.617	0.8785 ± 0.0302
PolarRec		✓	0.658 ± 0.243	26.225 ± 2.751	0.9002 ± 0.0268

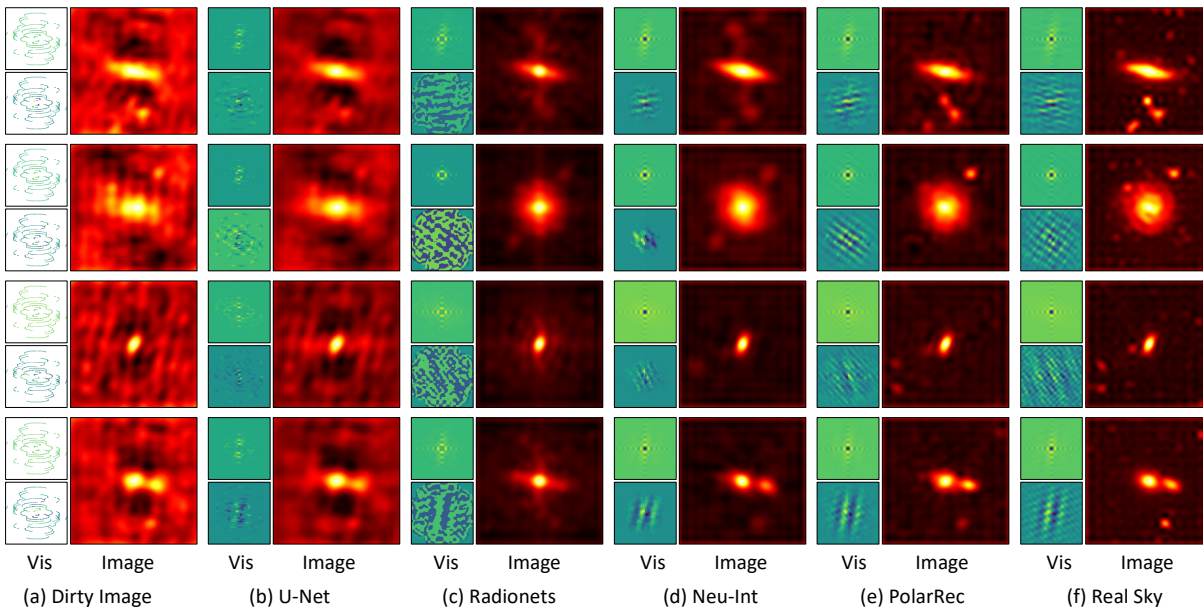


Figure 4: Visual comparison of visibility and image. The small panels to the left of each image are the corresponding visibility data, with the real part on top and the imaginary part at bottom.

Overall Comparison

We calculate the LFD, PSNR, and SSIM values for all test images reconstructed using our method and other methods, presenting both mean values and standard deviations. These results are tabulated in Table 1. The results show that PolarRec consistently outperforms the other methods in all three measures, LFD, PSNR and SSIM, underscoring the effectiveness of our reconstruction method.

We also present some representative reconstructed visibility and the corresponding images on the Galaxy10(DECals) dataset in Figure 4, including all deep-learning-based methods under comparison as well as the dirty images and the ground truth images of the real sky. Comparing the dirty images in Figure 4 (a) and the ground truth in Figure 4 (f), we find there are many artifacts and distortion of object structure in dirty images because of the sparsity of the visibility.

As shown in Figure 4 (b), reconstructions of the visibility by U-Net (Ronneberger, Fischer, and Brox 2015) are the worst, with artifacts dominating the resultant images. In Figure 4 (c), Radionets (Schmidt et al. 2022) are able to reconstruct more visibility content than U-Net. However, the

reconstruction is discontinuous. Although Radionets reduce artifacts in the imaging results, it cannot distinguish between separate sources that are in close proximity. Furthermore, many faint astronomical sources are missing in the reconstructed images. In contrast, as shown in Figure 4 (d), Neural Interferometry (Wu et al. 2022) (denoted Neu-Int) can continuously and realistically reconstruct the low-frequency components of the visibility, but misses much information from the high-frequency components, leading to a loss of details in the reconstruction.

The results of PolarRec (Figure 4 (e)) show that our method can effectively reconstruct more complete and continuous visibility data than others. The resultant imaging results not only eliminate artifacts but also restore the true structure of astronomical sources while preserving details and small faint sources.

Effect of Group Size

In this experiment, we vary the group size in number of visibility points and investigate its impact on the reconstruction results. We also record the inference latency of the encoding

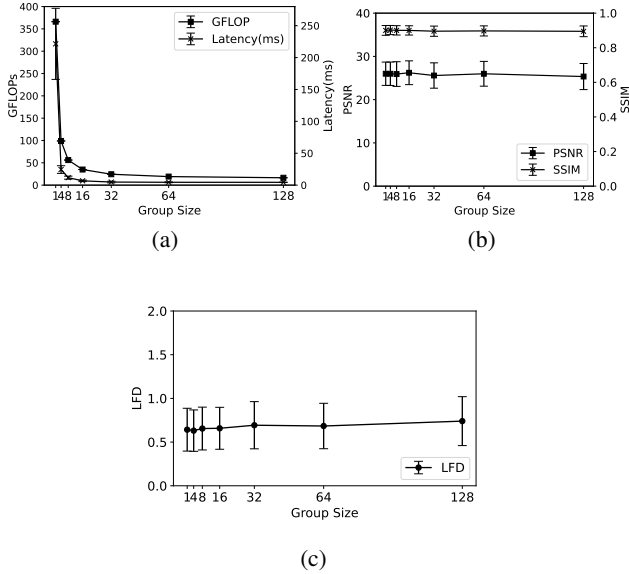


Figure 5: Effect of group size.

process, and use Floating Point Operations (FLOPs) to measure the computation cost. LFD, PSNR and SSIM are used to assess the reconstruction quality.

As illustrated in Figure 5, there is a sharp drop in both FLOPs and inference latency as the group size increases from 1 to 16. In contrast, the image quality in LFD, SSIM, and PSNR is almost constant. Between a group size of 64 to 128, there is a slight decrease in both PSNR and SSIM, while LFD shows a slight increase, implying that increasing group size beyond 64 might compromise the output quality. Moreover, when the group size is set to 1, it is the same as encoding at the granularity of individual points and the computation cost is the same as Neural Interferometry (Wu et al. 2022). The results indicate that encoding with group granularity as input to the transformer encoder is significantly more efficient than encoding at the point granularity.

Ablation Experiment of Weights in RFL

This ablation experiment aims to examine the significance of two weight matrices w_1 , w_2 in the Radial Frequency Loss by omitting them one at a time. The results in Table 2 confirm that the full Radial Frequency Loss is the best. Removing either component w_1 , or w_2 results in reduced performance

Table 2: Results of ablation experiments on RFL

Setting	Metrics		
	LFD↓	PSNR↑	SSIM↑
w/o w_1	0.727 (±0.228)	25.459 (±2.613)	0.8974 (±0.0267)
w/o w_2	0.722 (±0.272)	25.816 (±2.822)	0.8963 (±0.0289)
Full RFL	0.658 (±0.243)	26.225 (±2.751)	0.9002 (±0.0268)

across all metrics.

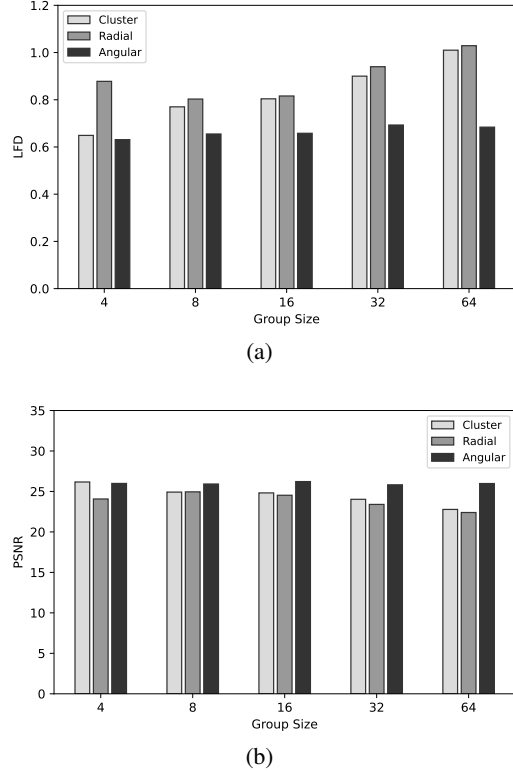


Figure 6: Effect of grouping method

Effect of grouping method

We also vary the grouping method and measure its performance impact on PolarRec. We implemented three grouping strategies: (1) grouping by clustering visibility points by their positions, (2) grouping by the radial coordinate, and (3) grouping by the angular coordinate. Each of these strategies was tested under various group sizes. The LFD and PSNR results are presented in Figure 6. Regardless of the group size, grouping the visibility points by angular coordinates always has the best performance. Especially when the group size increases, other methods tend to show a noticeable decline in PSNR and an increase in LFD, whereas grouping by the angular coordinate can effectively maintain faithful reconstruction results.

Conclusion and Future Work

We have presented PolarRec, introducing a polar coordinate representation to the reconstruction of interferometric visibility. By adopting angular and radial coordinates of visibility points, our method can reconstruct the visibility data with both effectiveness and efficiency. Our results show that PolarRec markedly improves imaging outcomes by faithfully reconstructing all frequency components of visibility while significantly reducing the computation cost, making it a practical solution for radio interferometric reconstruction applications. In the future, we will extend our method

to observations from a broader range of radio telescopes and extend this efficient visibility encoding process to tasks beyond reconstruction.

References

- [Ables 1974] Ables, J. 1974. Maximum entropy spectral analysis. *Astronomy and Astrophysics Supplement, Vol. 15*, p. 383–383.
- [Blum et al. 2016] Blum, R. D.; Burleigh, K.; Dey, A.; Schlegel, D. J.; Meisner, A. M.; Levi, M.; Myers, A. D.; Lang, D.; Moustakas, J.; Patej, A.; et al. 2016. The decam legacy survey. In *American Astronomical Society Meeting Abstracts# 228*, volume 228, 317–01.
- [Bouman et al. 2016] Bouman, K. L.; Johnson, M. D.; Zoran, D.; Fish, V. L.; Doeleman, S. S.; and Freeman, W. T. 2016. Computational imaging for vlbi image reconstruction. In *Proceedings of the IEEE Conference on Computer Vision and Pattern Recognition*, 913–922.
- [Bouman et al. 2018] Bouman, K. L.; Johnson, M. D.; Dalca, A. V.; Chael, A. A.; Roelofs, F.; Doeleman, S. S.; and Freeman, W. T. 2018. Reconstructing video of time-varying sources from radio interferometric measurements. *IEEE Transactions on Computational Imaging* 4(4):512–527.
- [Chael et al. 2018] Chael, A. A.; Johnson, M. D.; Bouman, K. L.; Blackburn, L. L.; Akiyama, K.; and Narayan, R. 2018. Interferometric imaging directly with closure phases and closure amplitudes. *The Astrophysical Journal* 857(1):23.
- [Chael et al. 2019] Chael, A. A.; Bouman, K. L.; Johnson, M. D.; Narayan, R.; Doeleman, S. S.; Wardle, J. F.; Blackburn, L. L.; Akiyama, K.; Wielgus, M.; Chan, C.-k.; et al. 2019. ehtim: Imaging, analysis, and simulation software for radio interferometry. *Astrophysics Source Code Library ascl-1904*.
- [Connor et al. 2022] Connor, L.; Bouman, K. L.; Ravi, V.; and Hallinan, G. 2022. Deep radio-interferometric imaging with polish: Dsa-2000 and weak lensing. *Monthly Notices of the Royal Astronomical Society* 514(2):2614–2626.
- [Dey et al. 2019] Dey, A.; Schlegel, D. J.; Lang, D.; Blum, R.; Burleigh, K.; Fan, X.; Findlay, J. R.; Finkbeiner, D.; Herrera, D.; Juneau, S.; et al. 2019. Overview of the desi legacy imaging surveys. *The Astronomical Journal* 157(5):168.
- [Dosovitskiy et al. 2021] Dosovitskiy, A.; Beyer, L.; Kolesnikov, A.; Weissenborn, D.; Zhai, X.; Unterthiner, T.; Dehghani, M.; Minderer, M.; Heigold, G.; Gelly, S.; et al. 2021. An image is worth 16x16 words: Transformers for image recognition at scale. In *Proceeding of the International Conference on Learning Representations*.
- [Henry 2021] Henry, L. 2021. Galaxy10 decals dataset. <https://github.com/henrysky/Galaxy10>.
- [Högbom 1974] Högbom, J. 1974. Aperture synthesis with a non-regular distribution of interferometer baselines. *Astronomy and Astrophysics Supplement Series* 15:417.
- [Hore and Ziou 2010] Hore, A., and Ziou, D. 2010. Image quality metrics: Psnr vs. ssim. In *2010 20th international conference on pattern recognition*, 2366–2369. IEEE.
- [Horn 1990] Horn, R. A. 1990. The hadamard product. In *Proc. Symp. Appl. Math*, volume 40, 87–169.
- [Jiang et al. 2021] Jiang, L.; Dai, B.; Wu, W.; and Loy, C. C. 2021. Focal frequency loss for image reconstruction and synthesis. In *Proceedings of the IEEE/CVF International Conference on Computer Vision*, 13919–13929.
- [Liu, Luo, and Wang 2022] Liu, H.; Luo, Q.; and Wang, F. 2022. Efficient radio interferometric imaging on the gpu. In *2022 IEEE 18th International Conference on e-Science (e-Science)*, 95–104. IEEE.
- [Paszke et al. 2019] Paszke, A.; Gross, S.; Massa, F.; Lerer, A.; Bradbury, J.; Chanan, G.; Killeen, T.; Lin, Z.; Gimelshein, N.; Antiga, L.; et al. 2019. Pytorch: An imperative style, high-performance deep learning library. *Advances in neural information processing systems* 32.
- [Perez et al. 2018] Perez, E.; Strub, F.; De Vries, H.; Dumoulin, V.; and Courville, A. 2018. Film: Visual reasoning with a general conditioning layer. In *Proceedings of the AAAI Conference on Artificial Intelligence*, volume 32.
- [Ronneberger, Fischer, and Brox 2015] Ronneberger, O.; Fischer, P.; and Brox, T. 2015. U-net: Convolutional networks for biomedical image segmentation. In *Medical Image Computing and Computer-Assisted Intervention—MICCAI 2015: 18th International Conference, Munich, Germany, October 5-9, 2015, Proceedings, Part III 18*, 234–241. Springer.
- [Schmidt et al. 2022] Schmidt, K.; Geyer, F.; Fröse, S.; Blumenkamp, P.-S.; Brüggem, M.; de Gasperin, F.; Elsässer, D.; and Rhode, W. 2022. Deep learning-based imaging in radio interferometry. *arXiv preprint arXiv:2203.11757*.
- [Silva et al. 2016] Silva, D. R.; Blum, R. D.; Allen, L.; Dey, A.; Schlegel, D. J.; Lang, D.; Moustakas, J.; Meisner, A. M.; Valdes, F.; Patej, A.; et al. 2016. The mayall z-band legacy survey. In *American Astronomical Society Meeting Abstracts# 228*, volume 228, 317–02.
- [Singh and Singh 2019] Singh, H., and Singh, H. 2019. Basics of python and scikit image. *Practical Machine Learning and Image Processing: For Facial Recognition, Object Detection, and Pattern Recognition Using Python* 29–61.
- [Sun and Bouman 2021] Sun, H., and Bouman, K. L. 2021. Deep probabilistic imaging: Uncertainty quantification and multi-modal solution characterization for computational imaging. In *Proceedings of the AAAI Conference on Artificial Intelligence*, volume 35, 2628–2637.
- [Tancik et al. 2020] Tancik, M.; Srinivasan, P.; Mildenhall, B.; Fridovich-Keil, S.; Raghavan, N.; Singhal, U.; Ramamoorthi, R.; Barron, J.; and Ng, R. 2020. Fourier features let networks learn high frequency functions in low dimensional domains. *Advances in Neural Information Processing Systems* 33:7537–7547.
- [Thompson, Moran, and Swenson 2017] Thompson, A. R.; Moran, J. M.; and Swenson, G. W. 2017. *Interferometry and synthesis in radio astronomy*. Springer Nature.
- [Vaswani et al. 2017] Vaswani, A.; Shazeer, N.; Parmar, N.; Uszkoreit, J.; Jones, L.; Gomez, A. N.; Kaiser, Ł.; and Poloz

sukhin, I. 2017. Attention is all you need. *Advances in neural information processing systems* 30.

[Wu et al. 2022] Wu, B.; Liu, C.; Eckart, B.; and Kautz, J. 2022. Neural interferometry: Image reconstruction from astronomical interferometers using transformer-conditioned neural fields. In *Proceedings of the AAAI Conference on Artificial Intelligence*.

[Zou et al. 2017] Zou, H.; Zhou, X.; Fan, X.; Zhang, T.; Zhou, Z.; Nie, J.; Peng, X.; McGreer, I.; Jiang, L.; Dey, A.; et al. 2017. Project overview of the beijing–arizona sky survey. *Publications of the Astronomical Society of the Pacific* 129(976):064101.